NANO LETTERS

pubs.acs.org/NanoLett

Letter

Uncovering Maximum Chirality in Resonant Nanostructures

Weijin Chen,[▽] Zhenyu Wang,[▽] Maxim V. Gorkunov,[▽] Jiazheng Qin, Ruize Wang, Chaowei Wang, Dong Wu, Jiaru Chu, Xuehua Wang, Yuri Kivshar,* and Yang Chen*

Cite This: *Nano Lett.* 2024, 24, 9643−9649

Read Online

ACCESS | Metrics & More | Article Recommendations | Supporting Information

ABSTRACT: Chiral nanostructures allow engineering of chiroptical responses; however, their design usually relies on empirical approaches and extensive numerical simulations. It remains unclear if a general strategy exists to enhance and maximize the intrinsic chirality of subwavelength photonic structures. Here, we suggest a microscopic theory and uncover the origin of strong chiral responses of resonant nanostructures. We reveal that the reactive helicity density is critically important for achieving maximum chirality at resonances. We demonstrate our general concept on the examples of planar photonic crystal slabs and metasurfaces, where out-of-plane mirror symmetry is broken by a bilayer design. Our findings provide a general recipe for designing photonic structures with maximum chirality, paving the way toward many applications, including chiral sensing, chiral emitters and detectors, and chiral quantum optics.

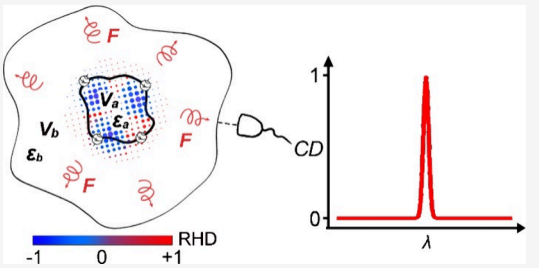

KEYWORDS: *Optical chirality, chiral metastructure, bound state in the continuum, circular dichroism*

Chirality, a fundamental property of nature, refers to the geometric attribute of an object lacking mirror-reflection symmetry.[1] An overwhelming majority of chemically and biologically active substances are chiral, such as amino acids, DNAs, and glucose. When interacting with circularly polarized light (CPL), chiral molecules exhibit chiroptical properties, which have been widely applied in drug development,[2] disease diagnosis,[3] asymmetric photochemistry,[4] and light field manipulation.[5] However, since the helical pitches of natural chiral molecules are much smaller than that of CPL, their chiroptical properties are very weak and thus hard to detect or harness.[1]

Artificial chiral nanostructures can achieve giant chiroptical responses due to the excitation of optical resonances.[6−12] Despite many different designs of chiral nanostructures, there still exists no general understanding of the origin of their chiroptical properties and systematic ways to enhance them, especially at the microscopic level. Intuitively, structural chirality will directly induce asymmetry of electromagnetic fields, but it remains unclear how to quantitatively evaluate such near-field chiral asymmetry and modulate it via delicate designs of structures and materials. Furthermore, it still remains uncertain how near-field chirality transfers to the far field, producing circular dichroism (CD) in radiation. As a consequence, the optimized design of chiral nanostructures heavily relies on wide-ranging and time-consuming numerical simulations, lacking an insightful guideline.

Recently, *chiral bound states in the continuum* (BICs) have been suggested to enable maximum chirality over a subwavelength thickness.[13−21] However, all of the existing chiral BIC structures have employed sophisticated three-dimensional (3D) geometries to simultaneously break in-plane and out-of-plane mirror symmetries, which inevitably leads to great challenges for conventional nanofabrication techniques. Consequently, many researchers have been forced to resort to special nanofabrication methods, such as slanted reactive ion etching,[17,18] multistep lithography,[19] and grayscale lithography,[20] which also set strict requirements for state-of-the-art facilities, accurate process control, and special nanostructure designs. Although two-dimensional (2D) planar BIC structures preserving out-of-plane mirror symmetry have been reported to exhibit strong CD, the CD resonance is attributed to extrinsic chirality[22] or anisotropy-induced polarization conversion,[23] but not the intrinsic chirality of the nanostructure. While optical structures require thickness for many optical operations,[24] it is still unclear if we can achieve intrinsic maximum chirality in planar structures without implementation of sophisticated out-of-plane fabrication.

In this Letter, we suggest a microscopic theory to shed light on the origin of chiral responses in resonant nanostructures associated with the generation of surface chiral charges at material boundaries. Although optical chirality density, also known as *active helicity density*, has been exclusively utilized to evaluate the chiral asymmetry of electromagnetic fields of

Received: May 22, 2024
Revised: June 28, 2024
Accepted: July 16, 2024
Published: July 23, 2024

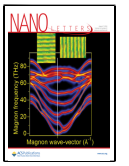

nanostructures,[25−30] we demonstrate, for the first time to our knowledge, the significant impact from *reactive helicity density* (RHD) in producing chiral radiation that could be dominant over optical chirality density. As proof of principle, we analyze two types of planar resonant systems, photonic crystal slabs and arrays of dielectric resonators composing metasurfaces. Based on microscopic theory, the structural and material parameters are delicately designed to modulate the RHD distributions of nanostructures, enabling maximum chirality.

First, we consider quasi-normal modes (QNMs) supported by resonant nanostructures in open space. The chiral degree of resonant radiation can be evaluated by the time-averaged chiral flux $\tilde{\mathbf{F}} = {}^{c}/_{4\omega} Im(\mathbf{E} \times \mathbf{D}^* + \mathbf{H} \times \mathbf{B}^*)$, where c is the light velocity and $\mathbf{E}/\mathbf{H}$ and $\mathbf{D}/\mathbf{B}$ are the electric/magnetic fields and electric displacement/magnetic induction, respectively.[31−33] The harmonic time dependence $e^{-i\omega t}$ is assumed with $\omega = \Omega - \Gamma i$ being the complex frequency, where Ω and Γ are the resonance frequency and decay rate. In the case of homogeneous, nonmagnetic ($\mu = \mu_0$), and lossless ($\varepsilon = \varepsilon^*$) media without nanostructures, the chiral flux follows the conservation law[34] (see Supporting Information):

$$\Gamma \cdot \tilde{\chi}_i + \nabla \cdot \tilde{\mathbf{F}} = 0 \quad (1)$$

where $\tilde{\chi}_i = {}^{c}/_{\omega} Im(\mathbf{B}^* \cdot \mathbf{D})$ is optical chirality density (OCD), also known as active helicity density. Such a conservation law is the application of Noether's theorem in electromagnetic duality symmetry, implying that chiral flux stems from the dissipation of OCD in homogeneous media.[33] In contrast, when considering nanostructures and their surrounding environments, multiple material regions are involved, and thus, the boundary effect has to be considered. In the simplest case where the nanostructure is composed of a material ε_a in the region V_a and surrounded by an environment material ε_b in the region V_b (Figure 1), we integrate eq 1 in the two regions,

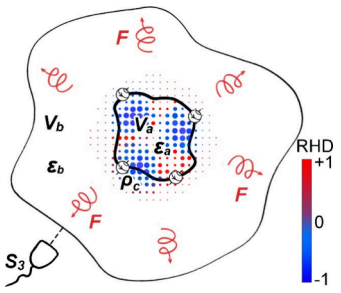

Figure 1. Illustration of the microscopic theory. The unbalanced reactive helicity density (RHD) in the near field of the resonator (V_a, ε_a) leads to far-field chiral flux $\mathbf{F}$ and generates radiative helicity S_3. Surface chiral charges ρ_c are induced on the material boundary acting as chiral sources.

apply the divergence theorem, and then subtract them to obtain (see Supporting Information):

$$\Gamma \cdot \iiint_{V_a \cup V_b} \tilde{\chi}_i \, dV + \oiint_{S_a} (\tilde{\mathbf{F}}_{S_a}^- - \tilde{\mathbf{F}}_{S_a}^+) \cdot \hat{\mathbf{n}} \, dS + \oiint_{S_b} \tilde{\mathbf{F}}_{S_b}^- \cdot \hat{\mathbf{n}} \, dS = 0, \quad (2)$$

where S_a and S_b are the closed surfaces of the volumes V_a and V_b and $\tilde{\mathbf{F}}_{S_b}^-$ is the radiated chiral flux. The boundary integration term $\oiint_{S_a} (\tilde{\mathbf{F}}_{S_a}^- - \tilde{\mathbf{F}}_{S_a}^+) \cdot \hat{\mathbf{n}} \, dS$ involves two chiral fluxes, $\tilde{\mathbf{F}}_{S_a}^-$ and $\tilde{\mathbf{F}}_{S_a}^+$, located respectively on the inner and outer surfaces of S_a, exhibiting discontinuity across the surface. In analogy to the definition of surface charge density ρ from $\mathbf{D}$, i.e., $\rho = (\mathbf{D}_S^- - \mathbf{D}_S^+) \cdot \hat{\mathbf{n}}$, we can also define surface chiral charge density ρ_c as $\rho_c = (\tilde{\mathbf{F}}_S^- - \tilde{\mathbf{F}}_S^+) \cdot \hat{\mathbf{n}}$, which acts as a chiral source and plays a crucial role in the generation of chiral radiation.

Further, the surface integral of chiral charges can be converted to a volume integral by using the divergence theorem, yielding $\oiint_{S_a} \rho_c \, dS = {}^{1}/_{2} (\varepsilon_a - \varepsilon_b)/\varepsilon_a \iiint_{V_a} (\Omega \cdot \tilde{\chi}_r - \Gamma \cdot \tilde{\chi}_i) \, dV$, where $\tilde{\chi}_r = {}^{c}/_{\omega} Re(B^* \cdot D)$ is reactive helicity density (RHD)[35,36] (see Supporting Information). Here, OCD and RHD are defined to possess the same dimension as angular momentum density.[33] Then, eq 2 is transformed to

$$\oiint_{S_b} \tilde{\boldsymbol{F}}_{S_b}^- \cdot \hat{\boldsymbol{n}} \, dS = \Pi(\mathrm{RHD}) + \Pi(\mathrm{OCD}), \quad (3)$$

where

$$\Pi(\mathrm{RHD}) = -\frac{1}{2} \frac{(\varepsilon_a - \varepsilon_b)}{\varepsilon_a} \Omega \iiint_{V_a} \tilde{\chi}_r \, dV$$

and

$$\Pi(\mathrm{OCD}) = -\Gamma \left[\iiint_{V_b} \tilde{\chi}_i \, dV + \frac{1}{2} \frac{(\varepsilon_a + \varepsilon_b)}{\varepsilon_a} \iiint_{V_a} \tilde{\chi}_i \, dV \right]$$

Considering the resonant system that is infinitely periodic in the $x-y$ plane, surface S_b can be chosen as two planes positioned above and below the system at a sufficiently large distance to eliminate the influence of evanescent fields. Meanwhile, if only one nondegenerate QNM is predominantly excited, the reciprocity theorem forces the radiation at these two planes to exhibit identical polarization states.[37] Then, the far-field radiative helicity of the resonance, characterized by the Stokes parameter S_3, is given by (see Supporting Information):

$$S_3 = \frac{\Omega}{P n_b} \oiint_{S_b} \tilde{\boldsymbol{F}}_{S_b}^- \cdot \hat{\boldsymbol{n}} \, dS = \frac{Q}{n_b} \left[\frac{\Pi(\mathrm{RHD})}{W} + \frac{\Pi(\mathrm{OCD})}{W} \right] = \frac{Q}{n_b} \left[\hat{\Pi}(\mathrm{RHD}) + \hat{\Pi}(\mathrm{OCD}) \right], \quad (4)$$

where P is the radiative power flux. $\hat{\Pi}(\mathrm{RHD})$ and $\hat{\Pi}(\mathrm{OCD})$ are normalized by the time-averaged energy stored in the system

$$W = \frac{1}{4} \iiint Re[\mathbf{E} \cdot \mathbf{D}^* + \mathbf{H} \cdot \mathbf{B}^*] \, dv$$

and the definition of quality (Q) factor $Q = \Omega W/P$ is also employed.

For the first time, to our knowledge, we have developed a microscopic theory to reveal that the far-field radiative helicity of a resonance S_3 is cooperatively determined by the volume integrations of RHD and OCD. In fact, OCD has long been considered the measure of the local chirality of electromagnetic fields, which act as the source of chiral flux. However, as revealed by our theory, this is only rigorously correct when the simplest case of homogeneous, nonmagnetic, and lossless media without nanostructures is considered. For the general case involving multiple material regions with the boundaries, the local chirality of electromagnetic fields is cooperatively determined by OCD and RHD, both of which act as the source of chiral flux. Furthermore, the contribution of RHD tends to be dominant over that of OCD in high-Q resonant systems according to their definitions (see Supporting Information). In addition, as suggested by eq 4, a high Q factor is beneficial for achieving strong chiroptical properties in resonant systems, which has long been ignored.

While our approach is valid for different types of resonances, here we consider the realization of maximum chirality based on high-Q BIC nanostructures.[38] The paradigm system is a photonic crystal slab (PCS) composed of an array of nanoholes in a bilayer dielectric slab (Figure 2a), which is immersed in a medium with $\varepsilon_0 = 2.1$. The bottom and top

https://doi.org/10.1021/acs.nanolett.4c02402
Nano Lett. 2024, 24, 9643−9649

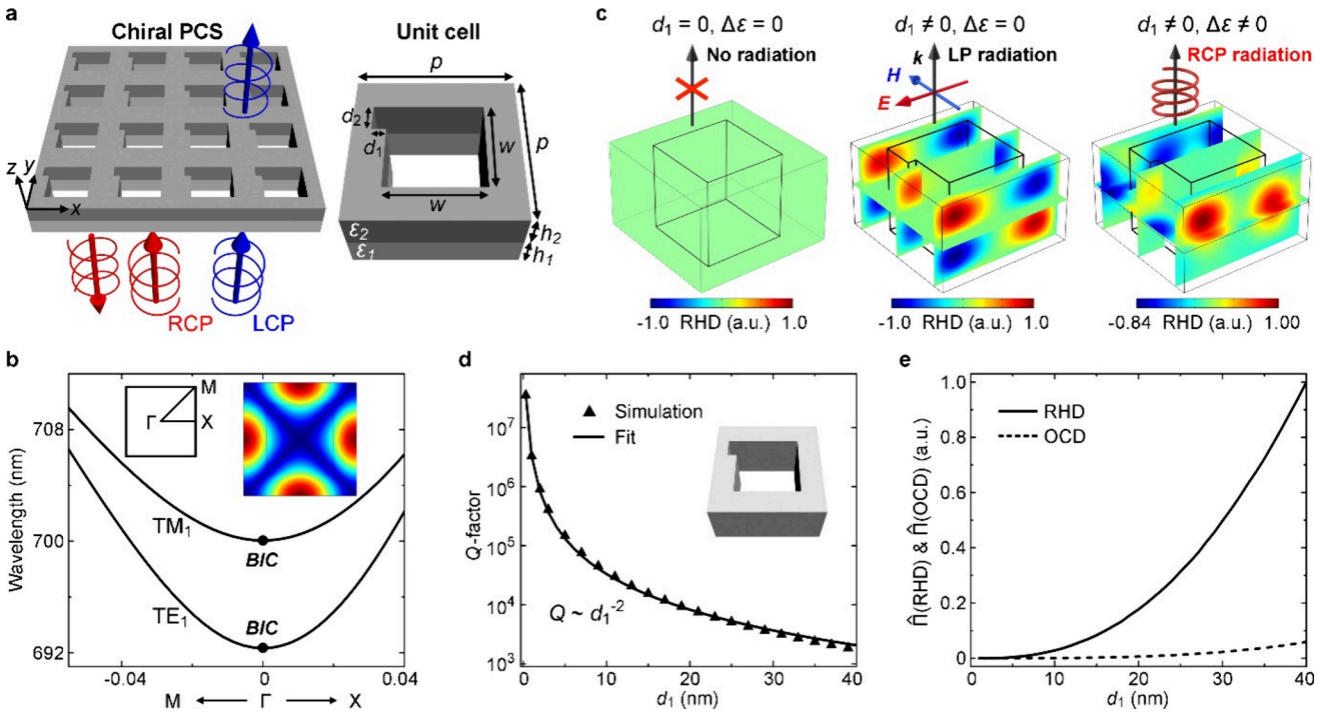

Figure 2. (a) Schematic of the bilayer PCS for realizing maximum chirality. The structural parameters are p = 340 nm, w = 200 nm, h_1 = 100 nm, h_2 = 111 nm, d_1 = 20 nm, d_2 = 80 nm, ε_1 = 6.72, and ε_2 = 9. (b) Band structure of the PCS (d_1 = 0, $\Delta\varepsilon$ = 0). The mode profile of TM_1 is shown in the inset. (c) RHD distributions for different combinations of d_1 and $\Delta\varepsilon$ with no radiation (left), LP radiation (middle), and RCP radiation (right). (d) Simulated Q factors of TM_1 as a function of the parameter d_1, fitted by the inversely quadratic law. (e) $\hat{\Pi}$(RHD) and $\hat{\Pi}$(OCD) integrated over the upper half space as functions of the parameter d_1.

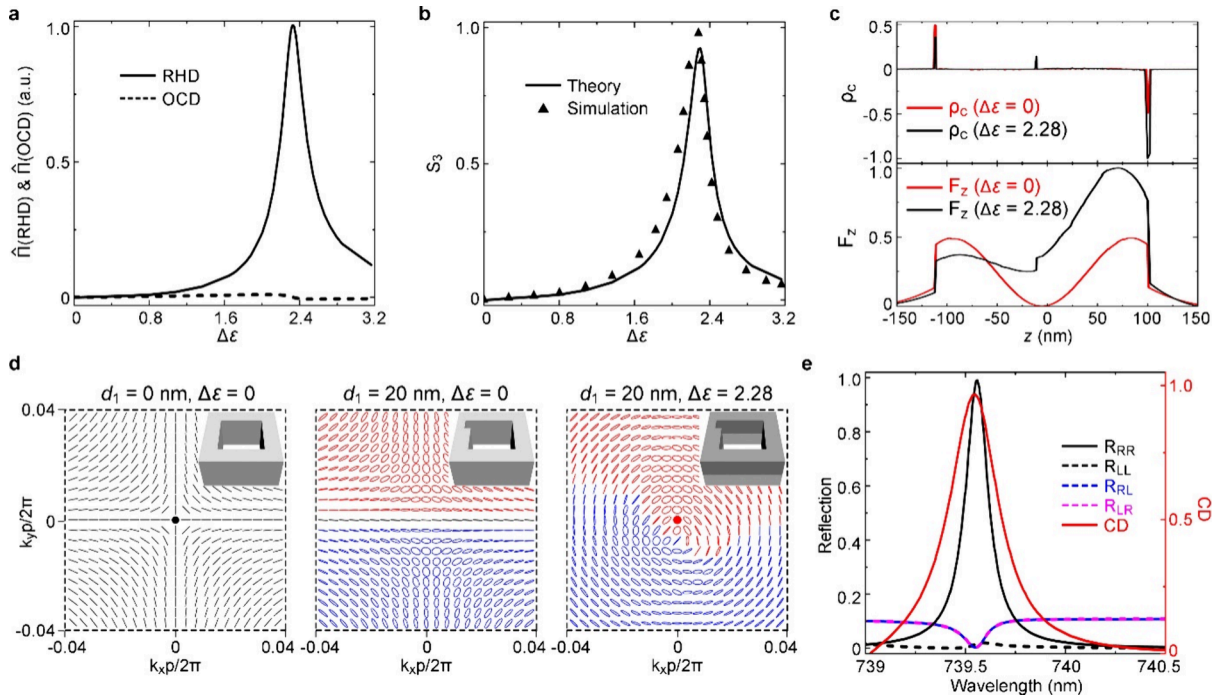

Figure 3. (a) $\hat{\Pi}$(RHD) and $\hat{\Pi}$(OCD) calculated for different $\Delta\varepsilon$. The permittivity of the bottom layer ε_1 is fixed as 6.72. (b) Radiative helicity S_3 for different $\Delta\varepsilon$, as retrieved by simulations and eq 4 of our theory. (c) Distributions of outgoing chiral flux $\mathbf{F}_z$ and surface chiral charge ρ_c plotted along the z direction for $\Delta\varepsilon$ = 0 and $\Delta\varepsilon$ = 2.28. (d) Evolution of eigenpolarization maps for different combinations of d_1 and $\Delta\varepsilon$. The black lines represent linear polarizations, while the ellipses of red (blue) color represent right-handed (left-handed) states. (e) Simulated reflection spectra of the chiral PCS in the circular basis, along with the retrieved CD spectrum. The notation R_{RL} refers to the reflection of the RCP component under LCP incidence.

layer has a permittivity of ε_1 and ε_2 and a thickness of h_1 and h_2, respectively. This structure is evolved from the typical monolayer PCS of square nanoholes by introducing an in-plane geometric deformation $d_1 \times d_2$ and an out-of-plane

https://doi.org/10.1021/acs.nanolett.4c02402
Nano Lett. 2024, 24, 9643−9649

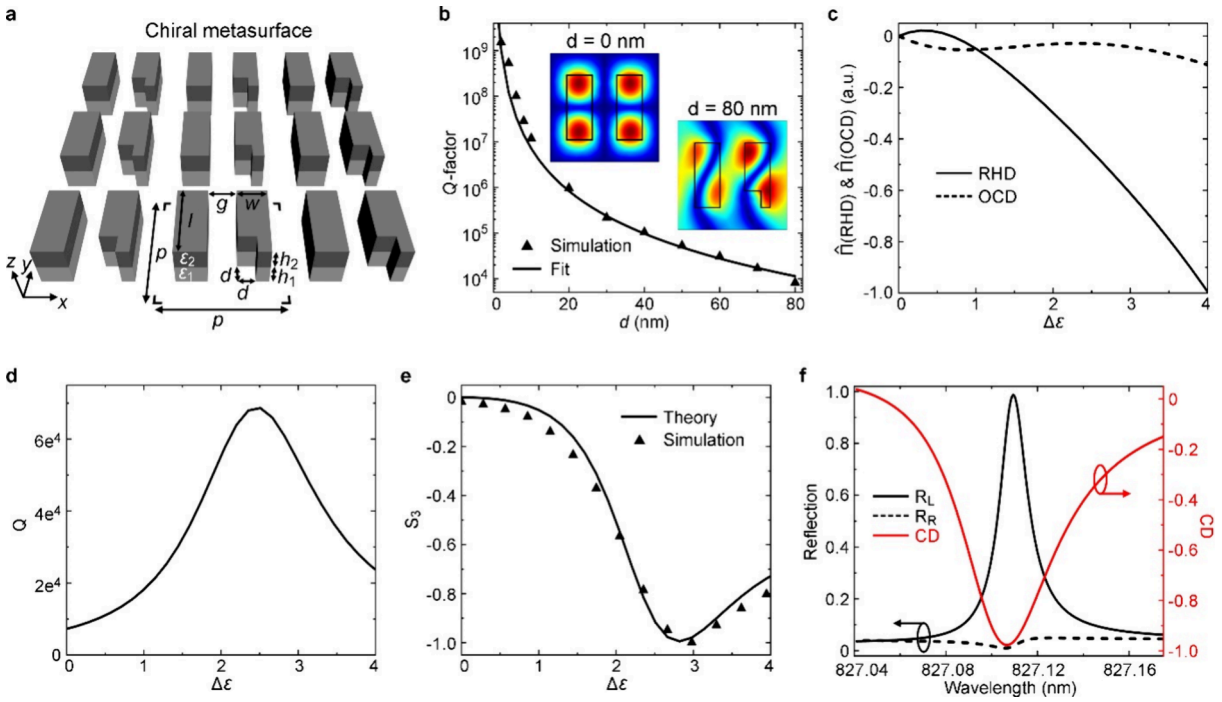

Figure 4. (a) Schematic of the bilayer metasurface for achieving maximum chirality. The structural parameters are p = 500 nm, w = 120 nm, l = 300 nm, h_1 = 110 nm, h_2 = 102 nm, g = 110 nm, ε_1 = 10.5, and ε_2 = 13.5. (b) Simulated Q factors as a function of the parameter d, fitted by the inversely quadratic law. The mode profiles for d = 0 and 80 nm are shown in the inset. (c) $\hat{\Pi}$(RHD) and $\hat{\Pi}$(OCD) calculated for different $\Delta\varepsilon$. The permittivity of the bottom layer ε_1 is fixed as 10.5. (d) Mode Q factor as a function of $\Delta\varepsilon$. (e) Radiative helicity S_3 for different $\Delta\varepsilon$ retrieved from simulations and eq 4 of our theory. (f) Reflection spectra of the chiral bilayer metasurface under RCP and LCP incidence, and the corresponding CD spectrum.

permittivity asymmetry $\Delta\varepsilon = \varepsilon_2 - \varepsilon_1$, so that all of the mirror symmetries are broken. A series of Bloch modes are supported by the PCS. For the fundamental TM_1 mode, a symmetry-protected BIC is supported at the Γ point of Brillouin zone when both the perturbations are absent ($d_1 = 0$, $\Delta\varepsilon = 0$), due to the C_2^z symmetry of the structure (Figure 2b). Its mode profile is shown in the inset. For the lossless BIC, the electromagnetic near fields are linearly polarized (LP) owing to time reversal symmetry,[17] and the retrieved RHD is zero over the structure (Figure 2c).

Once an in-plane perturbation is introduced, the BIC is converted to a quasi-BIC, whose Q factor obeys an inversely quadratic law on perturbation width d_1: $Q \sim d_1^{-2}$, as shown in Figure 2d. Here Q is calculated by $Q = \Omega/(2\Gamma)$, where the resonance frequency Ω and decay rate Γ are retrieved from simulations. The structural asymmetry directly induces the chirality of electromagnetic near fields, resulting in a nonzero RHD over the structure. Since RHD is a parity-odd scalar, it exhibits antisymmetric distributions relative to the central x−y plane, and the corresponding S_3 equals zero to generate LP radiation according to eq 4. If the in-plane structural asymmetry is further enhanced by a larger d_1, the corresponding near fields will become more chiral. This can be clearly observed by integrating $\hat{\Pi}$(RHD) and $\hat{\Pi}$(OCD) over the upper half space (Figure 2e), both of which are monotonically increased with d_1, but their integrations over the whole space will still maintain zero. In addition, we can also observe in Figure 2e that $\hat{\Pi}$(RHD) is much larger than $\hat{\Pi}$(OCD), implying the dominant contribution of RHD in producing chiral radiation.

Further, in order to break the out-of-plane balance of RHD, permittivity asymmetry $\Delta\varepsilon$ is introduced, resulting in chiral radiation (Figure 2c). The permittivity of the bottom layer ε_1 is fixed as 6.72. To select an optimal $\Delta\varepsilon$ for achieving maximum chirality, microscopic theory is exploited as a guideline. We calculate $\hat{\Pi}$(RHD) and $\hat{\Pi}$(OCD) as functions of $\Delta\varepsilon$ and observe that $\hat{\Pi}$(RHD) first increases rapidly with $\Delta\varepsilon$ and then decreases, peaking at $\Delta\varepsilon$ = 2.33 (Figure 3a). Additionally, the contribution of RHD is dominant over that of the OCD, leading to the radiative helicity of S_3 following a similar dependence on $\Delta\varepsilon$ as shown in Figure 3b. The maximum near-unity S_3 is reached when $\Delta\varepsilon$ is around 2.28, and the simulation results agree well with the theoretical results based on eq 4. Thus, it is possible to quantitatively calculate the radiation polarization by considering the RHD according to our proposed theory. If the permittivity of the bottom layer ε_1 takes different values, both ε_2 and $\Delta\varepsilon$ should change accordingly to achieve the maximum S_3. Next, we examine the distributions of outgoing chiral flux $\mathbf{F}_z$ and surface chiral charge ρ_c along the z direction. As anticipated, $\mathbf{F}_z$ is continuous except on the material boundaries, where nonzero ρ_c appears (Figure 3c). For the case of $\Delta\varepsilon = 0$, ρ_c on the upper and lower surfaces of the structure is oppositely valued, and their generated chiral radiation combines to be LP in the far field. If $\Delta\varepsilon \neq 0$, unbalanced chiral charges will accumulate to produce chiral radiation.

Further, momentum-space eigenpolarization maps for different d_1's and $\Delta\varepsilon$'s are analyzed in Figure 3d, where BIC is presented as a polarization vortex singularity at the Γ point. The permittivity of the bottom layer ε_1 is fixed as 6.72. Once a nonzero d_1 is induced, the at-Γ BIC singularity is evolved to an LP quasi-BIC, and a pair of half-charged C points with right-handed and left-handed circular polarization (RCP and LCP) are observed in the momentum space.[22,39] When $\Delta\varepsilon$ = 2.28 is

https://doi.org/10.1021/acs.nanolett.4c02402
Nano Lett. 2024, 24, 9643−9649

further introduced, the C+ point is shifted to the Γ point (Figure 3d), indicating the realization of the maximum chirality. This is also confirmed by the simulated reflection spectra in the circular basis under normal incidence (Figure 3e). We can see that the chiral PCS is strongly coupled to RCP light showing a sharp R_{RR} resonance at 739.56 nm, while it is transparent for LCP incidence showing negligible R_{LL}. The cross-polarized components R_{RL} and R_{LR} are zero, implying the absence of polarization conversion, which is an important criterion for intrinsic maximum chirality.[13] CD defined as CD = $(R_R - R_L)/(R_R + R_L)$ is calculated to be up to 0.97 (Figure 3e). The simulated transmission spectra are provided in Figure S3. In this way, we have presented an alternative strategy to control the radiative helicity S_3 and achieve maximum chirality in a more flexible way, as compared to the existing 3D-structure approaches.[13−20] During fabrication, we can just select two materials from the list of available dielectrics (e.g., Si/SiN in ref 40) and prepare a bilayer membrane. Then, according to their thicknesses and permittivities, we can adjust the 2D structure designs for maximizing CD, which are readily accessible for electron beam lithography, focused ion beam etching, and nanoprinting.

Next, we realize maximum chirality in arrays of dielectric resonant nanoparticles to further demonstrate the universality of our theory (Figure 4a). The band structure of the metasurface is provided in the Supporting Information. When a nonzero d is introduced to convert the BIC at around 813 nm to a quasi-BIC, its Q factor rapidly decreases with d (Figure 4b). Since all the in-plane mirror symmetry of the structure is broken, the mode profile is evolved from a symmetric pattern to a chiral twisted one (Figure 4b, inset), but the corresponding RHD distributions are still antisymmetric with respect to the central $x-y$ plane (see Supporting Information). Thus, a nonzero $\Delta\varepsilon$ is further required, and the dependence of $\hat{\Pi}$(RHD) and $\hat{\Pi}$(OCD) on $\Delta\varepsilon$ is plotted in Figure 4c, showing again the dominant role of RHD. The permittivity of the bottom layer ε_1 is fixed as 10.5. In this case, $\hat{\Pi}$(RHD) approximately exhibits a monotonic increase with $\Delta\varepsilon$, but the Q factor of quasi-BIC exhibits a resonance feature that peaked at $\Delta\varepsilon = 2.51$ (Figure 4d). Then, as determined by eq 4, the maximum chirality (i.e., $S_3 = -1$) is achieved for $\Delta\varepsilon = 2.85$, which is consistent with simulation results (Figure 4e). The reflection spectra for RCP and LCP normal incidences (R_R and R_L) are simulated in Figure 4f. The reflection R_R vanishes at the wavelength of 827.11 nm, while R_L exhibits a sharp and near-unity peak, leading to a CD up to −0.97. The simulated transmission spectra are provided in Figure S4d.

In summary, we have developed a microscopic theory to uncover the origin of chiral responses in resonant nanostructures associated with the generation of surface chiral charges on material boundaries. We have revealed the significant contribution of reactive helicity density in producing chiral radiation, which could be dominant over the optical chirality density. As guided by the theory, we have proposed a general recipe to realize maximum chirality in planar nanostructures, such as PCSs and metasurfaces, which could find important applications in chiral sensing, circularly polarized emission and lasing, polarized photodetection, and quantum optics.

■ ASSOCIATED CONTENT

Supporting Information

The Supporting Information is available free of charge at https://pubs.acs.org/doi/10.1021/acs.nanolett.4c02402.

Differential form of conservation law for optical chirality density, integral form of the conservation law, conversion of surface-integrated chiral charges into a volume integral, the relation of S_3 and chiral flux, details of numerical simulations, transmission spectra for the chiral photonic crystal slab, dependence of $\Delta\varepsilon$ on ε_1 for maximum S_3, and supplementary results for the chiral metasurface are available (PDF)

■ AUTHOR INFORMATION

Corresponding Authors

Yuri Kivshar − *Nonlinear Physics Centre, Research School of Physics, Australian National University, Canberra, Australian Capital Territory 2601, Australia;* orcid.org/0000-0002-3410-812X; Email: yuri.kivshar@anu.edu.au

Yang Chen − *Chinese Academy of Sciences Key Laboratory of Mechanical Behavior and Design of Materials, Department of Precision Machinery and Precision Instrumentation, University of Science and Technology of China, 230027 Hefei, China;* orcid.org/0000-0002-8501-5417; Email: cyang_phys@ustc.edu.cn

Authors

Weijin Chen − *Chinese Academy of Sciences Key Laboratory of Mechanical Behavior and Design of Materials, Department of Precision Machinery and Precision Instrumentation, University of Science and Technology of China, 230027 Hefei, China; Department of Electrical and Computer Engineering, National University of Singapore, 117583 Singapore, Singapore*

Zhenyu Wang − *Chinese Academy of Sciences Key Laboratory of Mechanical Behavior and Design of Materials, Department of Precision Machinery and Precision Instrumentation, University of Science and Technology of China, 230027 Hefei, China*

Maxim V. Gorkunov − *Shubnikov Institute of Crystallography, NRC "Kurchatov Institute", 119333 Moscow, Russia; National Research Nuclear University MEPhI, 115409 Moscow, Russia;* orcid.org/0000-0002-0461-243X

Jiazheng Qin − *Department of Electrical and Computer Engineering, National University of Singapore, 117583 Singapore, Singapore*

Ruize Wang − *Chinese Academy of Sciences Key Laboratory of Mechanical Behavior and Design of Materials, Department of Precision Machinery and Precision Instrumentation, University of Science and Technology of China, 230027 Hefei, China*

Chaowei Wang − *Chinese Academy of Sciences Key Laboratory of Mechanical Behavior and Design of Materials, Department of Precision Machinery and Precision Instrumentation, University of Science and Technology of China, 230027 Hefei, China*

Dong Wu − *Chinese Academy of Sciences Key Laboratory of Mechanical Behavior and Design of Materials, Department of Precision Machinery and Precision Instrumentation, University of Science and Technology of China, 230027 Hefei, China;* orcid.org/0000-0003-0623-1515

Jiaru Chu − *Chinese Academy of Sciences Key Laboratory of Mechanical Behavior and Design of Materials, Department of Precision Machinery and Precision Instrumentation, University of Science and Technology of China, 230027 Hefei, China;* orcid.org/0000-0001-6472-8103

https://doi.org/10.1021/acs.nanolett.4c02402
Nano Lett. 2024, 24, 9643−9649

Xuehua Wang − *State Key Laboratory of Optoelectronic Materials and Technologies, School of Physics, Sun Yat-sen University, Guangzhou 510275, China;* orcid.org/0000-0003-1324-1471

Complete contact information is available at: https://pubs.acs.org/10.1021/acs.nanolett.4c02402

Author Contributions

[▽]These authors contributed equally to this work. Y.C. and Y.K. conceived the idea. Y.C., W.C., and M.V.G. developed the theory. Y.C., W.C., and Z.W. conducted the simulations and analyzed the results. Y.C. and Y.K. supervised the project. Y.C., W.C., and Y.K. wrote the manuscript with contributions from all coauthors.

Notes

The authors declare no competing financial interest.

■ ACKNOWLEDGMENTS

Y.C. acknowledges the support from the National Key Research and Development Project (Grant No. YF2100230012) and National Natural Science Foundation of China (Grant No. 62275241). J.Q. acknowledges financial support from the NRF, Prime Minister's Office, Singapore under the Competitive Research Program Award (NRF-CRP26-2021-0063). The work of M.G. was carried out within the State assignment of NRC "Kurchatov Institute". D.W. acknowledges support from the National Key Research and Development Project (Grant No. 2021YFF0502700) and National Natural Science Foundation of China (Grant No. 62325507, 61927814). Y.K. was supported by the Australian Research Council (grant DP210101292) and the International Technology Center Indo-Pacific (ITC IPAC) via Army Research Office (contract FA520923C0023). This work was partially carried out at the USTC Center for Micro and Nanoscale Research and Fabrication.

■ REFERENCES

(1) Barron, L. D. *Molecular Light Scattering and Optical Activity*; Cambridge University Press: Cambridge, 2004.
(2) Leung, D.; Kang, S. O.; Anslyn, E. V. Rapid determination of enantiomeric excess: a focus on optical approaches. *Chem. Soc. Rev.* **2012**, *41*, 448−479.
(3) Kumar, J.; Erana, H.; López-Martínez, E.; Claes, N.; Martín, V. F.; Solís, D. M.; Bals, S.; Cortajarena, A. L.; Castilla, J.; Liz-Marzán, L. M. Detection of amyloid fibrils in Parkinson's disease using plasmonic chirality. *Proc. Natl. Acad. Sci. U. S. A.* **2018**, *115*, 3225−3230.
(4) He, C.; Yang, G.; Kuai, Y.; Shan, S.; Yang, L.; Hu, J.; Zhang, D.; Zhang, Q.; Zou, G. Dissymmetry enhancement in enantioselective synthesis of helical polydiacetylene by application of superchiral light. *Nat. Commun.* **2018**, *9*, 5117.
(5) Ghosh, A.; Fischer, P. Chiral molecules split light: reflection and refraction in a chiral liquid. *Phys. Rev. Lett.* **2006**, *97*, No. 173002.
(6) Papakostas, A.; Potts, A.; Bagnall, D. M.; Prosvirnin, S. L.; Coles, H. J.; Zheludev, N. I. Optical manifestations of planar chirality. *Phys. Rev. Lett.* **2003**, *90*, No. 107404.
(7) Gansel, J. K.; Thiel, M.; Rill, M. S.; Decker, M.; Bade, K.; Saile, V.; von Freymann, G.; Linden, S.; Wegener, M. Gold helix photonic metamaterial as broadband circular polarizer. *Science* **2009**, *325*, 1513−1515.
(8) Collins, J. T.; Kuppe, C.; Hooper, D. C.; Sibilia, C.; Centini, M.; Valev, V. K. Chirality and chiroptical effects in metal nanostructures: fundamentals and current trends. *Advanced Optical Materials* **2017**, *5*, No. 1700182.
(9) Hentschel, M.; Schäferling, M.; Duan, X.; Giessen, H.; Liu, N. Chiral plasmonics. *Science advances* **2017**, *3*, No. e1602735.
(10) Chen, Y.; Du, W.; Zhang, Q.; Avalos-Ovando, O.; Wu, J.; Xu, Q.-H.; Liu, N.; Okamoto, H.; Govorov, A. O.; Xiong, Q.; Qiu, C.-W. Multidimensional nanoscopic chiroptics. *Nature Reviews Physics* **2022**, *4*, 113−124.
(11) Wang, S.; Wen, S.; Deng, Z.-L.; Li, X.; Yang, Y. Metasurface-based solid poincaré sphere polarizer. *Phys. Rev. Lett.* **2023**, *130*, No. 123801.
(12) Zhang, X.; Cui, T. J. Artificial intelligence-assisted chiral nanophotonic designs. *Opto-Electronic Advances* **2023**, *6*, No. 230057.
(13) Fernandez-Corbaton, I.; Fruhnert, M.; Rockstuhl, C. Objects of Maximum Electromagnetic Chirality. *Phys. Rev. X* **2016**, *6*, No. 031013.
(14) Dixon, J.; Lawrence, M.; Barton, D. R.; Dionne, J. Self-Isolated Raman Lasing with a Chiral Dielectric Metasurface. *Phys. Rev. Lett.* **2021**, *126*, No. 123201.
(15) Gorkunov, M. V.; Antonov, A. A.; Kivshar, Y. S. Metasurfaces with Maximum Chirality Empowered by Bound States in the Continuum. *Phys. Rev. Lett.* **2020**, *125*, No. 093903.
(16) Overvig, A.; Yu, N.; Alu, A. Chiral Quasi-Bound States in the Continuum. *Phys. Rev. Lett.* **2021**, *126*, No. 073001.
(17) Chen, Y.; Deng, H.; Sha, X.; Chen, W.; Wang, R.; Chen, Y.-H.; Wu, D.; Chu, J.; Kivshar, Y. S.; Xiao, S.; Qiu, C.-W. Observation of intrinsic chiral bound states in the continuum. *Nature* **2023**, *613*, 474−478.
(18) Zhang, X.; Liu, Y.; Han, J.; Kivshar, Y.; Song, Q. Chiral emission from resonant metasurfaces. *Science* **2022**, *377*, 1215−1218.
(19) Kühner, L.; Wendisch, F. J.; Antonov, A. A.; Bürger, J.; Hüttenhofer, L.; de S. Menezes, L.; Maier, S. A.; Gorkunov, M. V.; Kivshar, Y.; Tittl, A. Unlocking the out-of-plane dimension for photonic bound states in the continuum to achieve maximum optical chirality. *Light: Science & Applications* **2023**, *12*, 250.
(20) Lim, Y.; Seo, I. C.; An, S. C.; Kim, Y.; Park, C.; Woo, B. H.; Kim, S.; Park, H. R.; Jun, Y. C. Maximally chiral emission via chiral quasibound states in the continuum. *Laser Photonics Rev.* **2023**, *17*, No. 2200611.
(21) Tang, Y.; Liang, Y.; Yao, J.; Chen, M. K.; Lin, S.; Wang, Z.; Zhang, J.; Huang, X. G.; Yu, C.; Tsai, D. P. Chiral bound states in the continuum in plasmonic metasurfaces. *Laser & Photonics Reviews* **2023**, *17*, No. 2200597.
(22) Liu, W.; Wang, B.; Zhang, Y.; Wang, J.; Zhao, M.; Guan, F.; Liu, X.; Shi, L.; Zi, J. Circularly Polarized States Spawning from Bound States in the Continuum. *Phys. Rev. Lett.* **2019**, *123*, No. 116104.
(23) Shi, T.; Deng, Z. L.; Geng, G.; Zeng, X.; Zeng, Y.; Hu, G.; Overvig, A.; Li, J.; Qiu, C. W.; Alu, A.; Kivshar, Y. S.; Li, X. Planar chiral metasurfaces with maximal and tunable chiroptical response driven by bound states in the continuum. *Nat. Commun.* **2022**, *13*, 4111.
(24) Miller, D. A. B. Why optics needs thickness. *Science* **2023**, *379*, 41−45.
(25) Hendry, E.; Carpy, T.; Johnston, J.; Popland, M.; Mikhaylovskiy, R. V.; Lapthorn, A. J.; Kelly, S. M.; Barron, L. D.; Gadegaard, N.; Kadodwala, M. Ultrasensitive detection and characterization of biomolecules using superchiral fields. *Nat. Nanotechnol* **2010**, *5*, 783−7.
(26) Mohammadi, E.; Tavakoli, A.; Dehkhoda, P.; Jahani, Y.; Tsakmakidis, K. L.; Tittl, A.; Altug, H. Accessible Superchiral Near-Fields Driven by Tailored Electric and Magnetic Resonances in All-Dielectric Nanostructures. *ACS Photonics* **2019**, *6*, 1939−1946.
(27) Garcia-Guirado, J.; Svedendahl, M.; Puigdollers, J.; Quidant, R. Enhanced Chiral Sensing with Dielectric Nanoresonators. *Nano Lett.* **2020**, *20*, 585−591.
(28) Droulias, S.; Bougas, L. Absolute Chiral Sensing in Dielectric Metasurfaces Using Signal Reversals. *Nano Lett.* **2020**, *20*, 5960−5966.
(29) Chen, Y.; Chen, W.; Kong, X.; Wu, D.; Chu, J.; Qiu, C.-W. Can. weak chirality induce strong coupling between resonant states? *Phys. Rev. Lett.* **2022**, *128*, No. 146102.

(30) Solomon, M. L.; Saleh, A. A. E.; Poulikakos, L. V.; Abendroth, J. M.; Tadesse, L. F.; Dionne, J. A. Nanophotonic Platforms for Chiral Sensing and Separation. *Accounts of chemical research* **2020**, *53*, 588−598.
(31) Bliokh, K. Y.; Nori, F. Characterizing optical chirality. *Phys. Rev. A* **2011**, *83*, No. 021803.
(32) Poulikakos, L. V.; Gutsche, P.; McPeak, K. M.; Burger, S.; Niegemann, J.; Hafner, C.; Norris, D. J. Optical Chirality Flux as a Useful Far-Field Probe of Chiral Near Fields. *ACS Photonics* **2016**, *3*, 1619−1625.
(33) Cameron, R. P.; Barnett, S. M.; Yao, A. M. Optical helicity, optical spin and related quantities in electromagnetic theory. *New J. Phys.* **2012**, *14*, No. 053050.
(34) Tang, Y.; Cohen, A. E. Optical chirality and its interaction with matter. *Phys. Rev. Lett.* **2010**, *104*, No. 163901.
(35) Nieto-Vesperinas, M.; Xu, X. Reactive helicity and reactive power in nanoscale optics: Evanescent waves. Kerker conditions. Optical theorems and reactive dichroism. *Physical Review Research* **2021**, *3*, No. 043080.
(36) Bliokh, K. Y.; Kivshar, Y. S.; Nori, F. Magnetoelectric effects in local light-matter interactions. *Phys. Rev. Lett.* **2014**, *113*, No. 033601.
(37) Chen, W.; Yang, Q.; Chen, Y.; Liu, W. Extremize optical chiralities through polarization singularities. *Phys. Rev. Lett.* **2021**, *126*, No. 253901.
(38) Hsu, C. W.; Zhen, B.; Stone, A. D.; Joannopoulos, J. D.; Soljačić, M. Bound states in the continuum. *Nature Reviews Materials* **2016**, *1*, No. 16048.
(39) Yin, X.; Jin, J.; Soljacic, M.; Peng, C.; Zhen, B. Observation of topologically enabled unidirectional guided resonances. *Nature* **2020**, *580*, 467−471.
(40) Kruk, S. S.; Wang, L.; Sain, B.; Dong, Z.; Yang, J.; Zentgraf, T.; Kivshar, Y. Asymmetric parametric generation of images with nonlinear dielectric metasurfaces. *Nat. Photonics* **2022**, *16*, 561−565.

https://doi.org/10.1021/acs.nanolett.4c02402
Nano Lett. 2024, 24, 9643−9649